

Data-Driven Phenotyping of COVID-19 from Chest X-rays

Mohammad Tariqul Islam, Jason W. Fleischer*

Department of Electrical and Computer Engineering, Princeton University, NJ-08540, USA

E-mail: jasonf@princeton.edu

December 2023

Abstract. The global impact and persistence of the COVID-19 pandemic, claiming over six million lives, calls for a more prepared and resilient medical response. Phenotyping is a quick way to allocate resources according to a patient’s needs, potentially easing the burden on the hospitals and their staff. Here, we present an unsupervised data-driven phenotyping algorithm using a single chest x-ray image. Our analysis reveals two clusters of COVID-19: one situated in between normal and pneumonia x-rays and the other distinct from both. We then apply the categorization to multiple images from the same patient, extending the method to longitudinal studies of disease progression and patient recovery. The results give an immediate criterion for coronavirus triage and provide a methodology for respiratory diseases beyond COVID-19.

1. Introduction

The sudden emergence, rapid spread, and poor understanding of COVID-19 made it the most devastating medical crisis since the 1918-19 Spanish flu [1]. At the onset of the pandemic, computer vision researchers focused on detecting COVID-19 from radiological images, typically by collecting data from different sources for supervised learning [2, 3, 4, 5]. These models were limited by poor aggregation of data, improper evaluation of models, and the immature state of peer review [6]. As a result, proper computational models were not devised and tested until after COVID-19 overloaded healthcare systems. Even now, the community needs more generalizable methods to understand emerging diseases and their pathophysiology.

Phenotyping is a quick way to ease the burden on healthcare systems both by assisting triage and improving resource allocation and treatment [1, 7]. In the early stages of the pandemic, COVID-19 was often characterized like other coronavirus diseases, e.g., as Acute Respiratory Distress Syndrome (ARDS), consistent with pneumonia-like thickening of the lungs [8]. However, half of all patients present differently, with near-normal breathing mechanics, clearer lungs, and hypoxemia (caused by poor oxygen

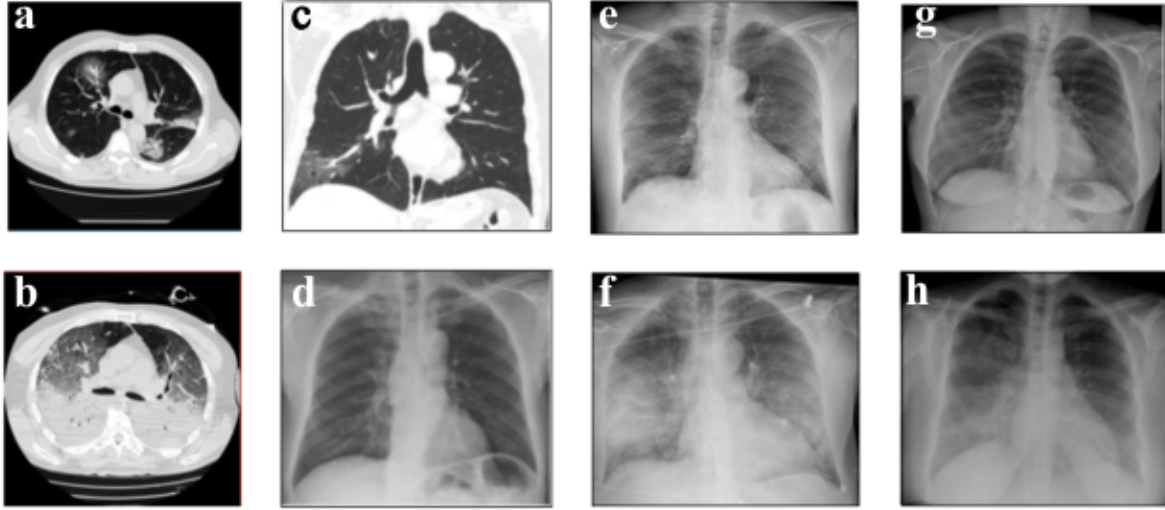


Figure 1. Computed tomography and x-ray data. (a,b) High-resolution CT images of COVID-19 patient at (a) admission to the hospital, (b) 7 days later [11]. (c) Posteroanterior CT and (d) x-ray images of the COVID-19 patient on the same day [16]. X-ray data of a COVID-19 patient at (e) admission, (f) 2 days later. (g) Normal x-ray. (h) x-ray of a patient with viral pneumonia [3].

transfer to the capillaries [9]). To distinguish, Gattinoni et al. [10, 11] suggested an ARDS-like H phenotype, characterized by *high* lung elastance, *high* weight, and *high* recruitment (potential to re-expand collapsed lung tissue, e.g. closed alveoli [12]); and an L phenotype in which corresponding measures are *low*. The former requires mechanical ventilation to survive, while the latter can precipitate a rapid worsening of ARDS through injured lungs due to high-pressure ventilation [13, 14]. Grasselli *et al.* [15] proposed phenotypes where *high* D-dimer concentration and *low* compliance increased mortality rate.

To date, the only way to confirm phenotypes is through high-resolution computed tomography (CT, Fig. 1). This is inhibitory for rapid triage and impossible for hospitals with limited resources. Here, we propose a method of phenotyping that uses only a single x-ray image.

That this is possible comes from the origin of CT: tomographic images are made from a collection of x-rays taken at different angles, each of which contains information on lung size, shape, and density. The resolution of CT images improves with the number of different views; higher resolution removes artifacts and provides cross-sections that allow visual separation of internal organs (Figs. 1a-c). The significance of this can be seen by comparing CT scans with individual x-ray images (Figs. 1d-h): each x-ray picture is a 2D projection of the 3D image, so that all internal features are superimposed. This overlap complicates diagnosis considerably, especially when disease forms around the heart and behind the breastbone. Nevertheless, frontal x-rays are the most frequent radiological tests performed in intensive care units [17] and are used often at the initial point of care to diagnose respiratory distress, e.g., pneumonia and chronic obstructive

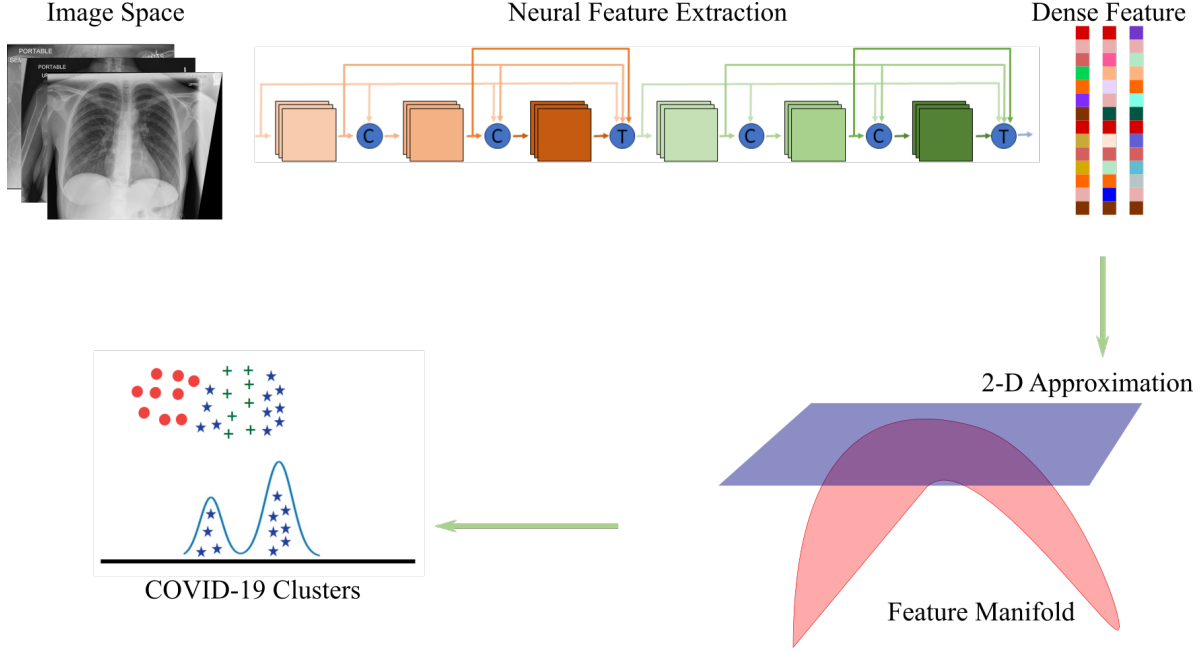


Figure 2. Schematic of the phenotyping process. X-ray features extracted from DenseNet-121 are compared and sorted. The results are then projected onto a 2D plane for visualization. All steps in the process are unsupervised.

pulmonary disease [18].

The images in Figs. 1d-h, taken from the publicly available COVIDx dataset [3], show representative chest x-rays from normal, pneumonia-positive [19], and COVID-19-positive patients [2]. Compared to a normal image, a pneumonia x-ray shows a diffuse pattern characteristic of fluid-filled lungs. Known as ground-glass opacities when translucent and consolidation when fully opaque, these regions form when an overstimulated immune system fills the alveoli with cells and fluid [20, 21]. Consequently, the location and density of these regions give many indications of the type and stage of the disease. Similar patterns are seen in COVID-19 patients [16], particularly as the illness progresses (Figs. 1b,d,f).

In this paper, we present an unsupervised method to phenotype COVID-19 patients. It works by reducing the dimensionality of the original chest x-rays into a smaller feature space of normal, pneumonia, and COVID-19 patients. The features are then further reduced to a 2D scatterplot using graph-based neighbor embedding. By leveraging prior patterns from normal and pneumonia cases, the algorithm reveals two distinct COVID-19 clusters: one that resembles a response between normal and pneumonia-positive patients, and one that is distinctly unique. Finally, we identify these data-driven clusters as COVID-19 phenotypes by checking the radiological reports and clinical notes associated with the x-rays.

2. Materials and Methods

Our machine learning pipeline, shown schematically in Fig. 2, consists of two steps:

- 1) Extracting features from x-rays, and
- 2) Embedding the features into a lower dimension using a dimensionality reduction method.

The first step makes the problem more manageable by discovering an effective basis and ameliorating variations in the patient image data, e.g., size, alignment, and acquisition protocols. However, this feature space is abstract and still rather high-dimensional, making it difficult to interpret. Step 2 reduces the dimensionality further, enabling easier visualization and classification. For simplicity, and to follow convention, we graph the final data as a scatterplot in two dimensions (2D) [22]. Below, we discuss the datasets and individual components of the pipeline.

2.1. Datasets

We explored two different COVID-19 databases: COVID-19 image data collection (COVIDC) [2] and RSNA international COVID-19 open radiology database (RICORD) [23]. These datasets, compiled from disparate sources (online vs. DICOM images), exhibit variations in sampling criteria, confounding factors, and labels. The RSNA pneumonia detection set (RSNA-PDC) [19] is the source of x-rays of normal and pneumonia-positive patients.

We first compared 97 posteroanterior (PA) x-rays from the COVIDC set with 308 normal and 308 pneumonia-positive x-rays from the RSNA-PDC dataset. Detailed information about the normal and pneumonia patients is unavailable, but there is some annotated information about COVID-19 patients. The 97 COVID-19 x-rays include 71 unique patients, of which 38 were male (53.5%), 23 were female (32.4%), and the rest were unlabeled. Of these 71 patients, 56 had entries containing age (median age 58.5 years). Of the 56 patients, 36 are male (58.5 years) and 20 are female (59.0 years). Here, we refer to the term ‘stage of illness’, a confounding factor, as the number of days passed after the onset of illness (entries: 75, 40 male, 21 female, median: 5 days).

In the second dataset, we combined 1096 x-rays from the RICORD dataset with 7966 normal and 5423 pneumonia-positive x-rays from the RSNA-PDC dataset. The 1096 COVID-19 x-rays include 351 unique patients, of which 208 (59.26%) are male (median age 57.84 years), and 143 (40.74%) are female (52.76 years). The dataset contains disease labels in 2 variables: the appearance of the patient and airspace disease grading [24]. The appearance classifications are

- 1) Typical: multifocal bilateral, peripheral opacities, and/or opacities with rounded morphology; lower lung-predominant distribution,
- 2) Intermediate: absence of typical findings and unilateral, central, or upper lung predominant distribution of airspace disease,

- 3) Atypical: pneumothorax or pleural effusion, pulmonary edema, lobar consolidation, solitary lung nodule or mass, diffuse tiny nodules, cavity, and
- 4) No Pneumonia.

The airspace disease grades are

- 1) Mild: opacities in 1 – 2 lung zones,
- 2) Moderate: opacities in 3 – 4 lung zones,
- 3) Severe: opacities in > 4 lung zones, and
- 4) No airspace disease

As multiple expert radiologists annotated the studies, we used the majority consensus to determine the labels. Additionally, we refer to the term ‘stage of illness’ for an x-ray as the number of days passed since the first one (of that patient).

2.2. Transformation and Preprocessing

Before clustering, we homogenize the datasets by applying the following transformations: image resizing, center cropping, and normalization. Images are resized such that the lowest dimension contains 256 pixels and then center-cropped to a 224×224 px² image for feature analysis. For Imagenet [25] pre-training, the normalization mean and standard deviation for RGB channels are (0.485, 0.456, 0.406) and (0.229, 0.224, 0.225), respectively.

2.3. Neural Network

We use a DenseNet-121 architecture [26] from the PyTorch deep learning library [27] pre-trained on the ImageNet database. The densely connected architecture reduces numerical instabilities originating from the depth of the network, while Imagenet pre-training ensures that the network is not biased by radiology-specific labels. We chose outputs from the final layer (before the softmax layer) as features, where the network is most discriminating. This approach is a standard practice in machine learning and medical image analysis [28, 29, 30, 31].

2.4. Dimensionality Reduction Algorithms

The goal for dimensionality reduction is to find a lower d-dimensional space so that the low-dimensional mapping matches the high-dimensional data. This matching is done by minimizing a loss function. We compared three different dimensionality reduction methods: principle component analysis (PCA), t-distributed stochastic neighbor embedding (t-SNE) [32], and uniform manifold approximation and projection (UMAP) [33]. PCA is a linear method that finds a set of orthogonal directions, ordered from maximum to minimum variance. It preserves large distances between points so that samples that are distinct from each other end up far apart. t-SNE and UMAP, on the other hand, are nonlinear and belong to the same class of ‘neighbor embedding’ algorithms.

Both have been prevalent in representation learning [34, 35], physics [36, 37, 38], and life sciences [22, 39].

The nonlinear algorithms consider a pairwise metric (usually Euclidean or correlation) between features that capture the topology of the dataset. Due to the nonlinearity, however, multiple realizations of the low-dimensional approximation can satisfy the constraints. In practice, the algorithms are run several times with varying parameters to find a consistent mapping [40, 41]. Further details are given in the supplementary materials.

2.5. Classification and Phenotyping

All the algorithms are unsupervised, in the sense that data labels are known but only provided afterward for visualization; they are not seen or used during clustering. The phenotype labels and the 1D projections of dimensionality-reduced data are obtained using a Gaussian mixture model [42].

3. Results

First, we do a detailed analysis of the COVIDC dataset. Then, we show additional insights from the analysis of the RICORD dataset.

3.1. COVID-19 Image Data Collection (COVIDC)

Figure 3 shows the results of PCA, tSNE, and UMAP for embedding features from the x-ray images. Figure 3(a) shows the output from PCA. The three labels significantly overlap among the points. Projection along the main principal component (Fig. 3(b)) gives a Gaussian profile for COVID-19 patients, a direct result of the broad statistics of the underlying data.

The t-SNE projection recognizes the large clusters of normal and pneumonia patients (Fig. 3c,d). Remarkably, however, this algorithm organizes COVID-19 features into two distinct clusters: one (in red ellipse) that resembles pneumonia and is situated away from the normal cluster and one between normal and pneumonia clusters.

We applied a second embedding algorithm, UMAP (3e,f), and observed the same clustering. Compared with the t-SNE plot, the UMAP plot is ‘cleaner’ and more compact, with a more uniform distribution of features, tighter groupings, and sharper boundaries between the x-ray types.

Unfortunately, the COVIDC dataset has no labels for any phenotypes. However, most chest x-rays have clinical notes on the stage of disease and response to treatment. This metadata, analyzed below, supports the phenotyping of the embedded data. Thus, we labeled the mappings of COVID-19 cases in t-SNE embedding into two phenotypes, i.e., Type I (75 samples, within normal and pneumonia clusters) and Type II (22 samples, isolated away from both). We then used these labels to color the UMAP (again, this is

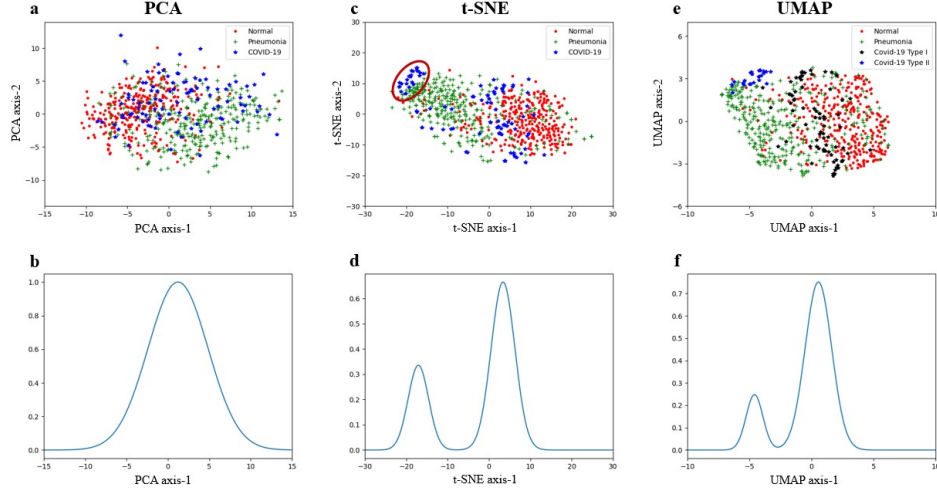


Figure 3. Clustering of frontal (PA) x-ray images of COVID-19 image data collection. Algorithms used: (a,b) PCA, (c,d) t-SNE, (e,f) UMAP. Top row: Scatter plots. Each sample point is an x-ray image and is labeled for visualization only; labels were not used for embedding. Bottom row: vertically integrated projections.

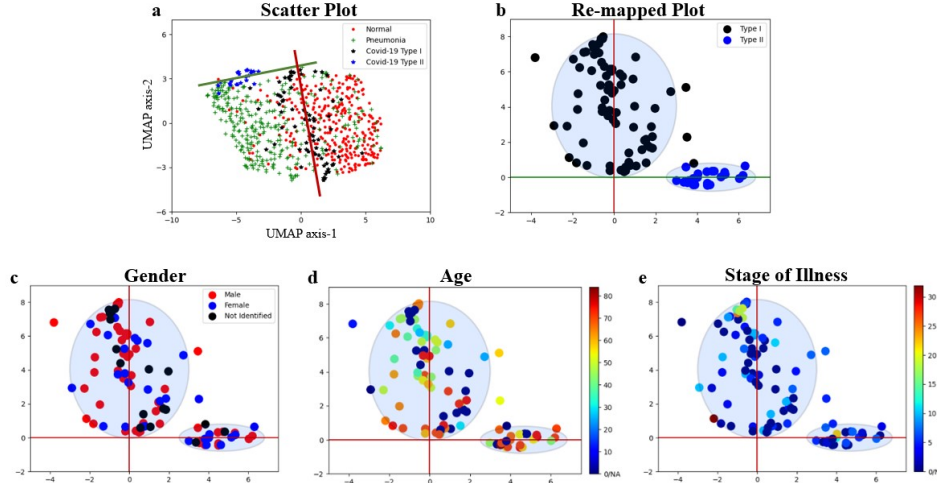


Figure 4. Classification of Type I and Type II phenotypes in UMAP. (a) Scatter plot showing principal axes of COVID-19. (b) Re-mapped plot using the principal axes. Confounding factors: (c) Gender, (d) Age, and (e) Stage of illness (measured in days from first hospitalization or sign of infection). Ellipse boundaries include 95% of samples.

for visualization purposes only and was not used by the algorithm). The consistency confirms that UMAP separates the same points as t-SNE but with a better mapping.

A provocative feature of both mappings is the isolation of the Type II x-rays from the pneumonia samples, indicating a unique signature of COVID-19 infection. Similarly, the placement of Type I patients between the reference ones is consistent with the simultaneous observations of normal breathing and low oxygenation levels [10, 14]. This rapid classification provides another visual metric that can summarize and complement

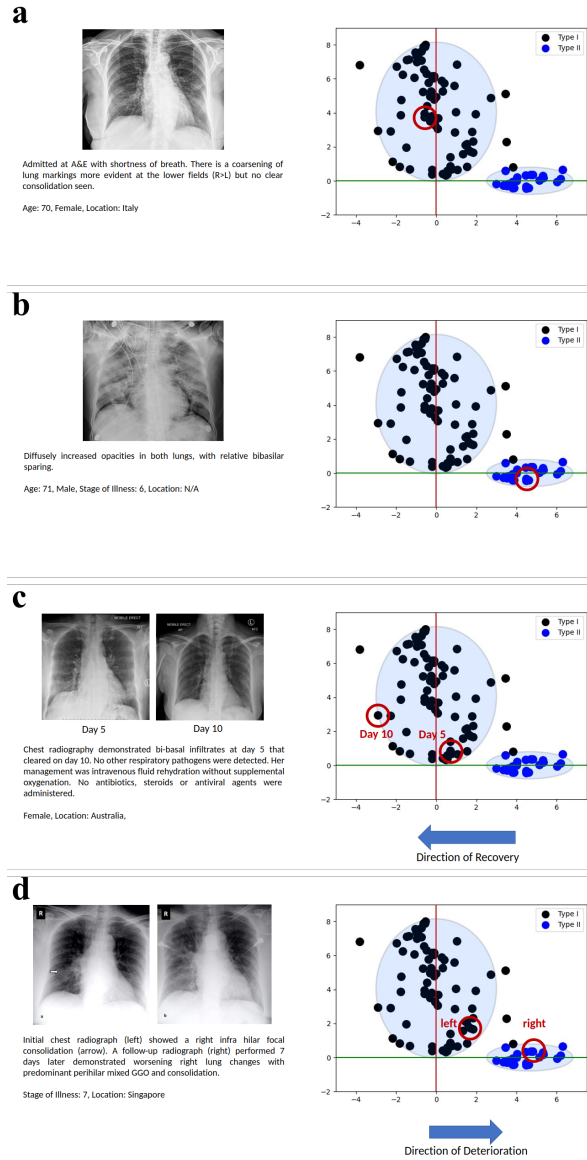


Figure 5. Individual samples from Fig. 4. Typical x-ray image within (a) Type I and (b) Type II clusters. Points move (c) from right to left for recovery and (d) from left to right as the patients worsen.

other patient data.

As UMAP provides a faster algorithm and more compact clusters along with a quantitative metric for the distance between pairs, we focus our analysis on the UMAP mapping. As a first step, we observe that the groupings in Fig. 3(e) (and in Fig. 4a) are nearly orthogonal; re-plotting the data in terms of these major axes gives a clear and easily describable representation (Fig. 4b). To aid in interpretation, we bound the two clusters by distinct ellipses, each containing 95% of their labels. The vertical Type I cluster is broader and more dispersed than the horizontal Type II cluster, with external points on both sides of its major axis. While the data is limited, several trends appear. Perhaps, most important, patient progression and recovery are captured (Fig. 5

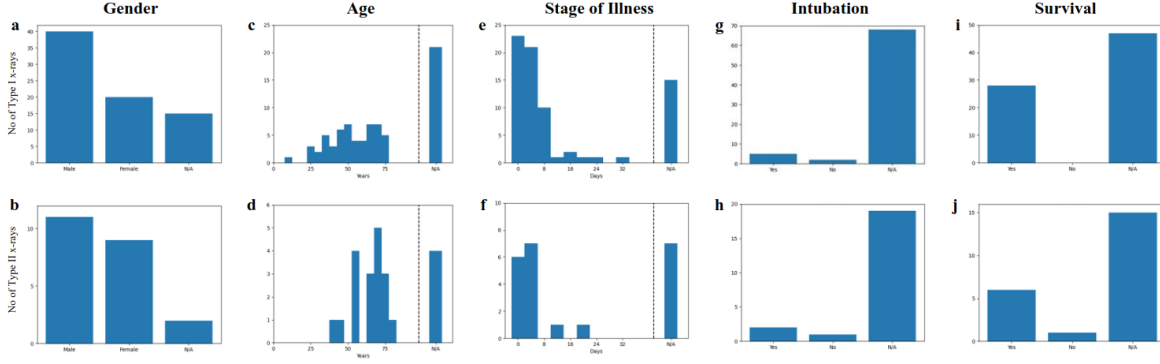


Figure 6. Histograms of confounding factors. Top row: Type I phenotype. Bottom row: Type II phenotype. There are more Type I than Type II patients, but their distributions are similar.

and supplementary): worsening condition appears as movement from left to right in parameter space (normal- to pneumonia-like, Fig. 5d), while improvement goes in the opposite direction (Fig. 5c). From the x-ray metadata [2], it was found that the isolated point (Fig. 4b) in the upper left is from the youngest patient in the dataset. The outlying point in the upper right has a partner x-ray image inside the Type I ellipse, taken from the same patient at an earlier time. The ‘misclassified’ point in the Type II cluster also has an earlier partner inside the Type I ellipse. The remaining external point, bisecting the ellipses, has ambiguous radiology and no clear marker suggesting outlier status.

A downside of this and all machine learning techniques is that it is unclear what the machine is learning. Here, it could be the presence and density of opacities [21], different rib thickness [43, 44] or heart size (from inflammation or strain[45]), or some other as-yet-unknown marker. Figures 4c-e show the scatterplot according to the confounding factors of gender, age, and stage of illness, while Figs. 6a-j show the corresponding distributions within the phenotypes. There are more males than females identified in the COVID-19 data, but they are dispersed in equal measure throughout the clusters (Fig. 4c). There are 40 (53.33%) males and 20 (26.67%) females in Type I cluster and 11 (50%) males and 9 (40.91%) females in Type II clusters; the rest of the x-rays do not have any gender label. Type II patients are (on average) 10 years older than Type I patients (Figs. 4d, 6c,d). The x-rays were taken at similar stages of development (Figs. 4e, 6e,f), with Type I and Type II average stage of illness being 6.15 and 5.66 days, respectively. Interestingly, both groups were intubated at a similar rate (6.67% and 9.09%, respectively; Figs. 6g,h), but all the Type I patients survived while only one Type II patient expired (Figs. 6i,j).

Scanning the clinical notes for disease markers reveals the core differences between the Type I and the Type II phenotypes (Table 1). The most common keyword of Type I phenotype is *fever* while it is *dyspnea* for Type II phenotype. Overall, Type II patients include disease markers that are severe in nature. The word *normal*, indicating normal-looking x-ray or blood works, appeared in 13.63% clinical notes for Type I phenotype

Table 1. Frequency of disease markers in the clinical notes of the COVID-19 patients.

Type I (No of Patients: 54, Comments: 66)		Type II (No of Patients: 21, Comments: 21)	
Word	Frequency	Word	Frequency
Fever	20 (30.30%)	Dyspnea	8 (38.10%)
Cough	19 (28.78%)	Thickening	7 (33.33%)
Opacity	17 (25.75%)	Fever	7 (33.33%)
Consolidation	13 (19.70%)	Consolidation	6 (28.57%)
Thickening	12 (18.18%)	Opacity	6 (28.57%)
Patchy	11 (16.67%)	Cough	5 (23.81%)
Ground-glass	10 (15.15%)	COPD	4 (19.05%)
Normal	9 (13.63%)	Ground-glass	4 (19.05%)
Pneumonia	9 (13.63%)	Effusion	4 (19.05%)
Infiltrates	8 (12.12%)	Hypoxic	2 (9.52%)
Dyspnea	3 (4.54%)	Pneumonia	2 (9.52%)

but only once for Type II phenotype. *COPD*, only appearing for Type II patients, was noted as patient history in all cases.

3.2. RSNA International COVID-19 Open Radiology Database (RICORD)

Figure 7 shows PCA, t-SNE, and UMAP embeddings and projections of RICORD data. The properties from Fig. 3, made with the previous dataset, are preserved, with the latter algorithms again separating the COVID patients into two distinct clusters. Similar to the previous results, we denoted the COVID-19 x-rays within the normal and pneumonia as Type I (283 samples) and the x-rays situated away from the normal representation as Type II (813 samples). Figure 8(a) shows the phenotypes from UMAP.

Figures 8(b-f) show the confounding factors in the scatterplot, and Figs. 9(a-e) show their distributions within Type I and Type II clusters. Overall, the labels of appearance classification (Figs. 8b and 9a,b) and airspace disease grading (Figs. 8c and 9c,d) again confirm our findings that Type II cluster indicates a more severe representation of COVID. Analysis of the metadata reveals that the clusters provide better sensitivity to airspace disease grading than appearance. In particular, 84.95%, 87.34%, and 88.98% are typical, intermediate, and atypical appearance and belong to the Type II cluster, whereas 78.67%, 89.88%, and 93.26% of mild, moderate, and severe airspace disease belong to the same.

Gender is equally dispersed in the clusters (Fig. 8d). Type I cluster contains a similar number of male and female patients (Fig. 9c), but the Type II cluster contains (153.48%) more male patients than female patients (Fig. 9c). This supports the observations that male patients suffer more severe cases of COVID-19 [46, 47].

Younger patients are located in the upper left region of the mapping (Fig. 8e), which matches that with the previous dataset. However, the rest of the population groups are

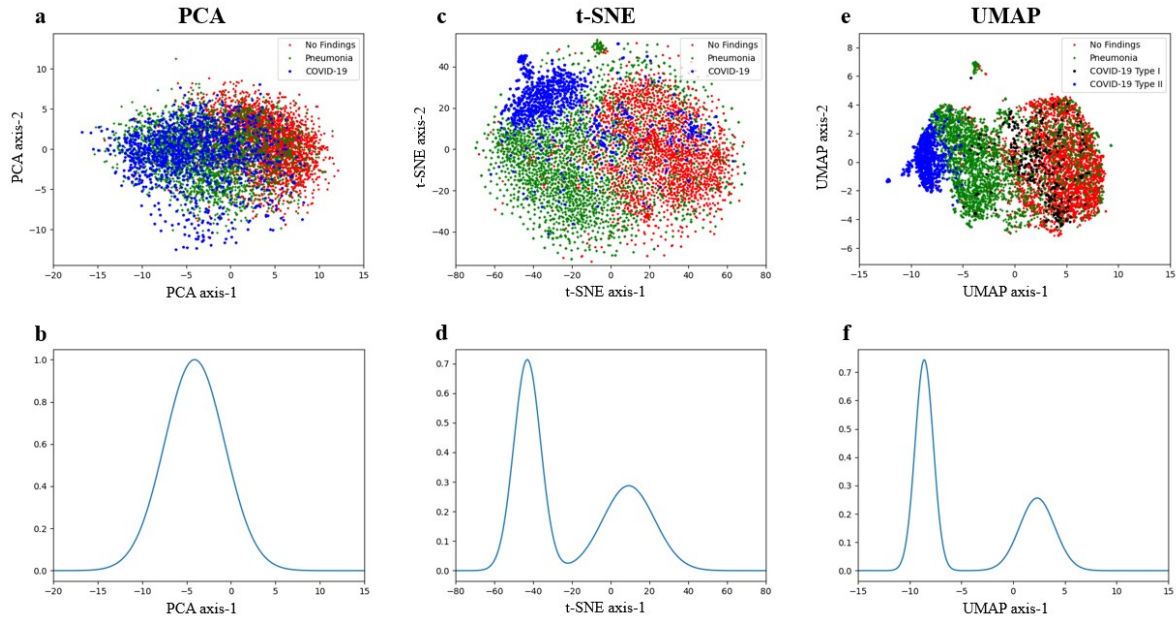


Figure 7. Clustering of frontal x-ray images of RICORD dataset. Algorithms used: (a,b) PCA, (c,d) t-SNE, (e,f) UMAP. Top row: Scatter plots. Each sample point is an x-ray image and is labeled for visualization only; labels were not used for embedding. Bottom row: vertically integrated projections.

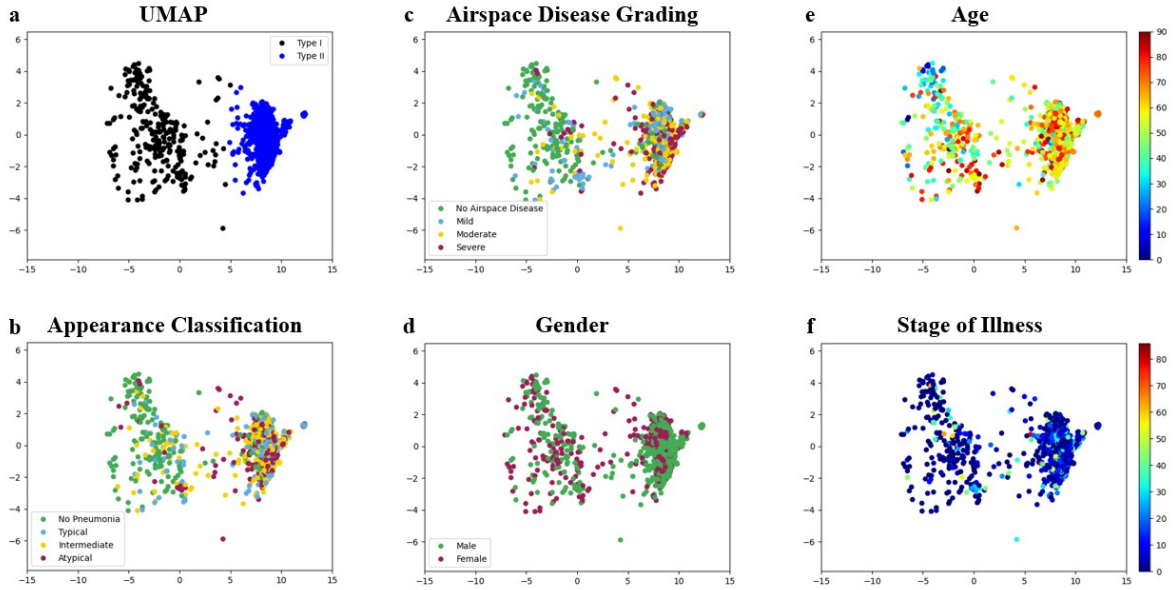


Figure 8. Classification of Type I and Type II phenotypes in UMAP. (a) Scatterplot labeled using Gaussian Mixture Model. Confounding factors: (b) Appearance classification, (c) Airspace disease grading, (d) Gender, (e) Age, and (f) Stage of illness (measured in days from the first x-ray).

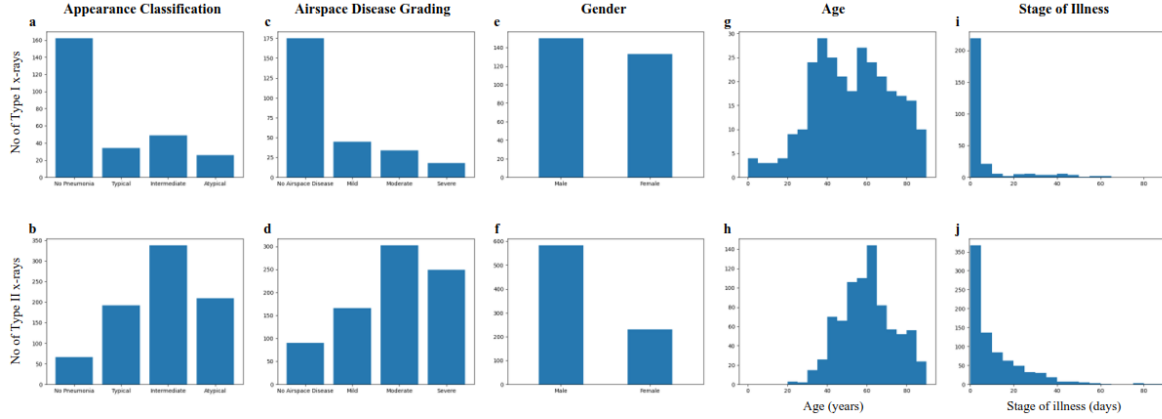


Figure 9. Histograms of confounding factors. Top row: Type I phenotype. Bottom row: Type II phenotype. There are more Type II than Type I patients. The Type I group has more patients with clear lungs, i.e., without pneumonia, whereas Type II patients predominantly have various degrees of opacity in the lungs.

spread with equal measure (Figs. 9g,h). ‘Stage of illness’ values are spread throughout the embeddings without any definite trends (Fig. 8f). Characteristically, Type I (mean: 6.75 days) patients had a shorter stage of illness than the more severely ill Type II (10.96 days) ones (Fig. 9i,j).

4. Discussion

Our unsupervised method of phenotyping COVID-19 involves two primary steps: extracting high-dimensional features from x-rays and using dimensionality reduction to obtain visualizable mappings. While the linear dimensionality reduction, PCA, failed to show any clustering tendencies within COVID-19 x-rays, the non-linear methods, t-SNE and UMAP, extracted two disparate populations: one positioned between the normal and pneumonia x-rays (Type I) and one that is distinct from both (Type II). The former captures early classification of the COVID-19 disease as a serious form of pneumonia, while the latter captures the unique signature that identifies COVID-19 as a new kind of disease [1]. To the best of our knowledge, this is the first work to propose phenotyping COVID-19 through dimensionality reduction.

We validated our approach using two sets: the smaller COVID-19 image data collection (97 x-rays) and the larger RICORD dataset (1096 x-rays). The first dataset was compiled during the initial wave of the pandemic and is sparse in confounding factors. Nevertheless, the analysis of the UMAP scatterplot (Fig. 4), distributions within the phenotypes (Fig. 6), and parsing of the clinical notes (Table 1) confirm two distinct phenotypes that provide a severity scale (Fig. 5). These phenotypes are confirmed again by analyzing the second dataset: RICORD (scatterplots in Fig. 8 and distributions of confounding factors in Fig. 9). This dataset was constructed retrospectively by grading the x-rays in terms of appearance and airspace disease. Characteristically, the Type

II phenotype indicates a more acute representation of COVID-19 disease with high sensitivity (93.26% for severe airspace disease). UMAP doesn't have a quantifiable global axis (unlike PCA), but we can potentially obtain quantitative results from the local relationship through UMAP's metric. Overall, our findings put forth unsupervised learning as a promising research direction not only for COVID-19 but also for other respiratory diseases yet to appear.

With the current data, it would be beneficial to repeat the study for more specific regions of interest and to use a wider range of metrics, e.g., structural similarity [48] and image statistics [49]. Likewise, it would help to leverage an additional viewpoint, such as the lateral (side) x-ray images commonly taken at the same time as the frontal view. Lateral x-rays are particularly useful for assessing the air spaces behind the breastbone and heart and provide an extreme form of limited-angle tomography [50], giving much-needed perspective for volume estimation. Finally, it is important to correlate the x-ray images with data from other observations as well [51], such as cardiovascular [45] and renal [52] metrics, the improvement of many patients via prone positioning (laying on the stomach) [53] and acoustic signatures of wheezing, gasping, and coughing [54, 55].

5. Conclusion

We proposed phenotyping COVID-19 disease from chest x-rays using dimensionality reduction. To this end, we employed neural features to reduce variabilities in the images and nonlinear dimensionality reduction to cluster the images into phenotypes. We hope that the results can serve as a guide for the classification of COVID-19 variants and for immediate triage and resource allocation for future respiratory diseases.

Acknowledgment

This research has been funded in part by a grant from the New Jersey Health Foundation. We also gratefully acknowledge financial support from the Schmidt DataX Fund at Princeton University made possible through a major gift from the Schmidt Futures Foundation.

Conflict of Interest Statement

The authors declare no conflict of interest.

Ethical Statement

There were no animal experiments or human participants in this study. Thus, no institutional review board approval is required.

Data Availability Statement

All the data used in this research are publicly available.

COVID-19 Image Data Collection can be accessed from:

<https://github.com/ieee8023/covid-chestxray-dataset>

RICORD dataset can be collected from:

<https://wiki.cancerimagingarchive.net/pages/viewpage.action?pageId=70230281>

COVIDx dataset can be accessed from:

<https://github.com/lindawangg/COVID-Net>

RSNA Pneumonia detection dataset can be accessed from:

<https://www.kaggle.com/c/rsna-pneumonia-detection-challenge/data>

References

- [1] Marcin F Osuchowski, Martin S Winkler, Tomasz Skirecki, Sara Cajander, Manu Shankar-Hari, Gunnar Lachmann, Guillaume Monneret, Fabienne Venet, Michael Bauer, Frank M Brunkhorst, et al. The covid-19 puzzle: deciphering pathophysiology and phenotypes of a new disease entity. *The Lancet Respiratory Medicine*, 9(6):622–642, 2021.
- [2] Joseph Paul Cohen, Paul Morrison, Lan Dao, Karsten Roth, Tim Q Duong, and Marzyeh Ghassemi. Covid-19 image data collection: Prospective predictions are the future. *arXiv preprint arXiv:2006.11988*, 2020.
- [3] Linda Wang, Zhong Qiu Lin, and Alexander Wong. Covid-net: A tailored deep convolutional neural network design for detection of covid-19 cases from chest x-ray images. *Scientific Reports*, 10(1):1–12, 2020.
- [4] Hanan Alghamdi, Ghada Amoudi, Salma Elhag, Kawther Saeedi, and Jomanah Nasser. Deep learning approaches for detecting covid-19 from chest x-ray images: A survey. *IEEE Access*, 2021.
- [5] Laure Wynants, Ben Van Calster, Gary S Collins, Richard D Riley, Georg Heinze, Ewoud Schuit, Marc MJ Bonten, Darren L Dahly, Johanna AA Damen, Thomas PA Debray, et al. Prediction models for diagnosis and prognosis of covid-19: systematic review and critical appraisal. *bmj*, 369, 2020.
- [6] Michael Roberts, Derek Driggs, Matthew Thorpe, Julian Gilbey, Michael Yeung, Stephan Ursprung, Angelica I Aviles-Rivero, Christian Etmann, Cathal McCague, Lucian Beer, et al. Common pitfalls and recommendations for using machine learning to detect and prognosticate for covid-19 using chest radiographs and ct scans. *Nature Machine Intelligence*, 3(3):199–217, 2021.
- [7] Lieuwe DJ Bos, Pratik Sinha, and Robert P Dickson. The perils of premature phenotyping in covid-19: a call for caution, 2020.
- [8] Marco Cascella, Michael Rajnik, Arturo Cuomo, Scott C Dulebohn, and Raffaella Di Napoli. Features, evaluation and treatment coronavirus (covid-19). *Statpearls [internet]*, 2020.
- [9] Jacob Herrmann, Vitor Mori, Jason HT Bates, and Béla Suki. Modeling lung perfusion abnormalities to explain early covid-19 hypoxemia. *Nature communications*, 11(1):4883, 2020.
- [10] Luciano Gattinoni, Silvia Coppola, Massimo Cressoni, Mattia Busana, Sandra Rossi, and Davide Chiumello. Covid-19 does not lead to a “typical” acute respiratory distress syndrome. *American journal of respiratory and critical care medicine*, 201(10):1299–1300, 2020.
- [11] Luciano Gattinoni, Davide Chiumello, Pietro Caironi, Mattia Busana, Federica Romitti, Luca Brazzi, and Luigi Camporota. Covid-19 pneumonia: different respiratory treatments for different phenotypes?, 2020.
- [12] G Mols, H-J Priebe, and J Guttman. Alveolar recruitment in acute lung injury. *British journal of anaesthesia*, 96(2):156–166, 2006.

- [13] Didier Dreyfuss and Georges Saumon. Ventilator-induced lung injury: lessons from experimental studies. *American journal of respiratory and critical care medicine*, 157(1):294–323, 1998.
- [14] Kyle-sidell, d. c. in webmd interview. <https://blogs.webmd.com/public-health/20200407/coronavirus-in-context-do-covid-19-vent-protocols-need-a-second-look>. Accessed: 2010-09-30.
- [15] Giacomo Grasselli, Tommaso Tonetti, Alessandro Protti, Thomas Langer, Massimo Girardis, Giacomo Bellani, John Laffey, Gianpaolo Carrafiello, Luca Carsana, Chiara Rizzuto, et al. Pathophysiology of covid-19-associated acute respiratory distress syndrome: a multicentre prospective observational study. *The lancet Respiratory medicine*, 8(12):1201–1208, 2020.
- [16] Ming-Yen Ng, Elaine YP Lee, Jin Yang, Fangfang Yang, Xia Li, Hongxia Wang, Macy Mei-sze Lui, Christine Shing-Yen Lo, Barry Leung, Pek-Lan Khong, et al. Imaging profile of the covid-19 infection: radiologic findings and literature review. *Radiology: Cardiothoracic Imaging*, 2(1):e200034, 2020.
- [17] Anusoumya Ganapathy, Neill KJ Adhikari, Jamie Spiegelman, and Damon C Scales. Routine chest x-rays in intensive care units: a systematic review and meta-analysis. *Critical Care*, 16(2):1–12, 2012.
- [18] Luciano Cardinale, Giovanni Volpicelli, Alessandro Lamorte, Jessica Martino, and Andrea Veltri. Revisiting signs, strengths and weaknesses of standard chest radiography in patients of acute dyspnea in the emergency department. *Journal of thoracic disease*, 4(4):398, 2012.
- [19] Rsna pneumonia detection challenge. <https://www.kaggle.com/c/rsna-pneumonia-detection-challenge/data>. Accessed: 2020-07-07.
- [20] David A Lynch, John D Newell, and Jin-Seong Lee. *Imaging of diffuse lung disease*. PMPH-USA, 2000.
- [21] Christopher E Engeler, Joseph H Tashjian, Stephen W Trenkner, and James W Walsh. Ground-glass opacity of the lung parenchyma: a guide to analysis with high-resolution ct. *AJR. American journal of roentgenology*, 160(2):249–251, 1993.
- [22] Dmitry Kobak and Philipp Berens. The art of using t-sne for single-cell transcriptomics. *Nature communications*, 10(1):1–14, 2019.
- [23] Emily B Tsai, Scott Simpson, Matthew Lungren, Michelle Hershman, Leonid Roshkovan, Errol Colak, Bradley J Erickson, George Shih, Anouk Stein, Jayshree Kalpathy-Cramer, et al. The rsna international covid-19 open annotated radiology database (ricord). *Radiology*, page 203957, 2021.
- [24] E. Tsai, S. Simpson, M.P. Lungren, M. Hershman, L. Roshkovan, E. Colak, B.J. Erickson, G. Shih, A. Stein, J. Kalpathy-Cramer, J. Shen, M.A.F. Hafez, S. John, P. Rajiah, B.P. Pogatchnik, J.T. Mongan, E. Altinmakas, E. Ranschaert, F.C. Kitamura, L. Topff, L. Moy, J.P. Kanne, and C Wu. Data from medical imaging data resource center (midrc) - rsna international covid radiology database (ricord) release 1c - chest x-ray, covid+ (midrc-ricord-1c), 2021.
- [25] Olga Russakovsky, Jia Deng, Hao Su, Jonathan Krause, Sanjeev Satheesh, Sean Ma, Zhiheng Huang, Andrej Karpathy, Aditya Khosla, Michael Bernstein, et al. Imagenet large scale visual recognition challenge. *International journal of computer vision*, 115(3):211–252, 2015.
- [26] Gao Huang, Zhuang Liu, Laurens Van Der Maaten, and Kilian Q Weinberger. Densely connected convolutional networks. In *Proceedings of the IEEE conference on computer vision and pattern recognition*, pages 4700–4708, 2017.
- [27] Adam Paszke, Sam Gross, Francisco Massa, Adam Lerer, James Bradbury, Gregory Chanan, Trevor Killeen, Zeming Lin, Natalia Gimelshein, Luca Antiga, et al. Pytorch: An imperative style, high-performance deep learning library. *Advances in neural information processing systems*, 32, 2019.
- [28] Hossein Azizpour, Ali Sharif Razavian, Josephine Sullivan, Atsuto Maki, and Stefan Carlsson. From generic to specific deep representations for visual recognition. In *Proceedings of the IEEE conference on computer vision and pattern recognition workshops*, pages 36–45, 2015.
- [29] Mohammad Tariqul Islam, Md Abdul Aowal, Ahmed Tahseen Minhaz, and Khalid Ashraf.

- Abnormality detection and localization in chest x-rays using deep convolutional neural networks. *arXiv preprint arXiv:1705.09850*, 2017.
- [30] Maithra Raghu, Chiyuan Zhang, Jon Kleinberg, and Samy Bengio. Transfusion: Understanding transfer learning for medical imaging. *Advances in neural information processing systems*, 32, 2019.
 - [31] Joseph Paul Cohen, Joseph D Viviano, Paul Bertin, Paul Morrison, Parsa Torabian, Matteo Guarrera, Matthew P Lungren, Akshay Chaudhari, Rupert Brooks, Mohammad Hashir, et al. Torchxrayvision: A library of chest x-ray datasets and models. In *International Conference on Medical Imaging with Deep Learning*, pages 231–249. PMLR, 2022.
 - [32] Laurens Van der Maaten and Geoffrey Hinton. Visualizing data using t-sne. *Journal of machine learning research*, 9(11), 2008.
 - [33] Leland McInnes, John Healy, and James Melville. Umap: Uniform manifold approximation and projection for dimension reduction. *arXiv preprint arXiv:1802.03426*, 2018.
 - [34] Taivanbat Badamdorj, Mrigank Rochan, Yang Wang, and Li Cheng. Contrastive learning for unsupervised video highlight detection. In *Proceedings of the IEEE/CVF Conference on Computer Vision and Pattern Recognition*, pages 14042–14052, 2022.
 - [35] Zifeng Wang, Zhenbang Wu, Dinesh Agarwal, and Jimeng Sun. Medclip: Contrastive learning from unpaired medical images and text. In *Proceedings of the 2022 Conference on Empirical Methods in Natural Language Processing*, pages 3876–3887, 2022.
 - [36] Michael Matty, Yi Zhang, T Senthil, and Eun-Ah Kim. Entanglement clustering for ground-stateable quantum many-body states. *Physical Review Research*, 3(2):023212, 2021.
 - [37] Benjamin WB Shires and Chris J Pickard. Visualizing energy landscapes through manifold learning. *Physical Review X*, 11(4):041026, 2021.
 - [38] Joana Teixeira, Vicente Rocha, João Oliveira, Pedro AS Jorge, and Nuno A Silva. Towards real-time identification of trapped particles with umap-based classifiers. In *Journal of Physics: Conference Series*, volume 2407, page 012043. IOP Publishing, 2022.
 - [39] Etienne Becht, Leland McInnes, John Healy, Charles-Antoine Dutertre, Immanuel WH Kwok, Lai Guan Ng, Florent Ginhoux, and Evan W Newell. Dimensionality reduction for visualizing single-cell data using umap. *Nature biotechnology*, 37(1):38–44, 2019.
 - [40] George C Linderman, Manas Rachh, Jeremy G Hoskins, Stefan Steinerberger, and Yuval Kluger. Fast interpolation-based t-sne for improved visualization of single-cell rna-seq data. *Nature methods*, 16(3):243–245, 2019.
 - [41] Dmitry Kobak and George C Linderman. Initialization is critical for preserving global data structure in both t-sne and umap. *Nature biotechnology*, 39(2):156–157, 2021.
 - [42] Christopher M Bishop. Pattern recognition. *Machine learning*, 128(9), 2006.
 - [43] Selma Uysal Ramadan, Nursel Türkmen, N Anıl Dolgun, Dilek Gökharman, Ritesh G Menezes, Mahmut Kacar, and Uğur Koşar. Sex determination from measurements of the sternum and fourth rib using multislice computed tomography of the chest. *Forensic Science International*, 197(1-3):120–e1, 2010.
 - [44] Ashley A Weaver, Samantha L Schoell, and Joel D Stitzel. Morphometric analysis of variation in the ribs with age and sex. *Journal of anatomy*, 225(2):246–261, 2014.
 - [45] Ying-Ying Zheng, Yi-Tong Ma, Jin-Ying Zhang, and Xiang Xie. Covid-19 and the cardiovascular system. *Nature Reviews Cardiology*, 17(5):259–260, 2020.
 - [46] Catherine Gebhard, Vera Regitz-Zagrosek, Hannelore K Neuhauser, Rosemary Morgan, and Sabra L Klein. Impact of sex and gender on covid-19 outcomes in europe. *Biology of sex differences*, 11:1–13, 2020.
 - [47] Nicola Lott, Caroline E Gebhard, Susan Bengs, Ahmed Haider, Gabriela M Kuster, Vera Regitz-Zagrosek, and Catherine Gebhard. Sex hormones in sars-cov-2 susceptibility: key players or confounders? *Nature Reviews Endocrinology*, 19(4):217–231, 2023.
 - [48] Zhou Wang, Alan C Bovik, Hamid R Sheikh, and Eero P Simoncelli. Image quality assessment: from error visibility to structural similarity. *IEEE transactions on image processing*, 13(4):600–612,

- 2004.
- [49] Yaotian Wang, Xiaohang Sun, and Jason Fleischer. When deep denoising meets iterative phase retrieval. In *International Conference on Machine Learning*, pages 10007–10017. PMLR, 2020.
 - [50] Nicolas C Pégard, Marton L Toth, Monica Driscoll, and Jason W Fleischer. Flow-scanning optical tomography. *Lab on a Chip*, 14(23):4447–4450, 2014.
 - [51] Chaolin Huang, Yeming Wang, Xingwang Li, Lili Ren, Jianping Zhao, Yi Hu, Li Zhang, Guohui Fan, Jiuyang Xu, Xiaoying Gu, et al. Clinical features of patients infected with 2019 novel coronavirus in wuhan, china. *The lancet*, 395(10223):497–506, 2020.
 - [52] Yichun Cheng, Ran Luo, Kun Wang, Meng Zhang, Zhixiang Wang, Lei Dong, Junhua Li, Ying Yao, Shuwang Ge, and Gang Xu. Kidney disease is associated with in-hospital death of patients with covid-19. *Kidney international*, 97(5):829–838, 2020.
 - [53] William R Henderson, Donald EG Griesdale, Paolo Dominelli, and Juan J Ronco. Does prone positioning improve oxygenation and reduce mortality in patients with acute respiratory distress syndrome? *Canadian respiratory journal*, 21(4):213–215, 2014.
 - [54] Udantha R Abeyratne, Vinayak Swarnkar, Amalia Setyati, and Rina Triasih. Cough sound analysis can rapidly diagnose childhood pneumonia. *Annals of biomedical engineering*, 41(11):2448–2462, 2013.
 - [55] Thomas F Quatieri, Tanya Talkar, and Jeffrey S Palmer. A framework for biomarkers of covid-19 based on coordination of speech-production subsystems. *IEEE Open Journal of Engineering in Medicine and Biology*, 1:203–206, 2020.